

www.acsami.org Research Article

Evolution of the Dynamic Solid Electrolyte Interphase in Mg Electrolytes for Rechargeable Mg-Ion Batteries

Shengqi Fan, Saida Cora, and Niya Sa*



Cite This: ACS Appl. Mater. Interfaces 2022, 14, 46635–46645



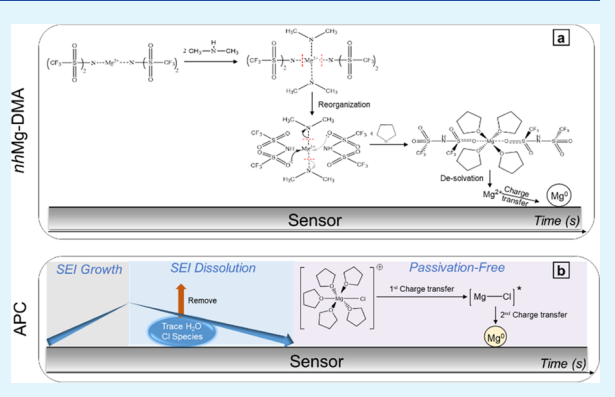
ACCESS I

III Metrics & More

Article Recommendations

s Supporting Information

ABSTRACT: Formation and evolution of the microscopic solid electrolyte interphase (SEI) at the Mg electrolyte/electrode interface are less reported and need to be completely understood to overcome the compatibility challenges at the Mg anode—electrolyte. In this paper, SEI evolution at the Mg electrolyte/electrode interface is investigated via an in situ electrochemical quartz crystal microbalance with dissipation mode (EQCM-D), electrochemical impedance spectroscopy (EIS), field emission scanning electron microscopy (FESEM), energy-dispersive X-ray spectroscopy (EDS), and Fourier transform infrared spectrometry (FTIR). Results reveal remarkably different interfacial evolutions for the two Mg electrolyte systems that are studied, a non-halogen Mg(TFSI)₂ electrolyte in THF with DMA as a cosolvent (nhMg-DMA electrolyte) versus a halogen-containing all-phenyl



complex (APC) electrolyte. The *nh*Mg-DMA electrolyte reports a minuscule SEI formation along with a significant Coulomb loss at the initial electrochemical cycles owing to an electrolyte reconstruction process. Interestingly, a more complicated SEI growth is observed at the later electrochemical cycles accompanied by an improved reversible Mg deposition attributed to the newly formed coordination environment with Mg²⁺ and ultimately leads to a more homogeneous morphology for the electrochemically deposited Mg⁰, which maintains a MgF₂-rich interface. In contrast, the APC electrolyte shows an extensive SEI formation at its initial electrochemical cycles, followed by a SEI dissolution process upon electrochemical cycling accompanied by an improved coulombic efficiency with trace water and chloride species removed. Therefore, it leads to SEI stabilization progression upon further electrochemical cycling, resulting in elevated charge transport kinetics and superior purity of the electrochemically deposited Mg⁰. These outstanding findings augment the understanding of the SEI formation and evolution on the Mg interface and pave a way for a future Mg-ion battery design.

KEYWORDS: multivalent batteries, solid electrolyte interphase, Mg electrolyte, electrochemical quartz crystal microbalance with dissipation

■ INTRODUCTION

Rechargeable magnesium batteries have received considerable attention in recent years due to their high volumetric capacity (3832 mAh/cm³), high abundance in the Earth's crust, and environmentally benign nature. Intriguing merits of rechargeable Mg batteries have served as a strong motivation for scientists to design electrolyte formulations from halogenfree elements with better chemical stability. However, the utilization of non-halogen magnesium electrolytes is restricted by the formed passivation films at the electrolyte/anode, which block Mg ion migration. Therefore, investigating the properties of the solid electrolyte interphase (SEI) is not trivial and plays a pivotal role in the development of Mg electrolytes that can achieve reversible Mg plating/stripping while maintaining the electrochemical and chemical stability.

The most easily obtained halogen-free electrolyte is a magnesium bis(trifluoromethanesulfonyl) imide $[Mg(TFSI)_2]$ -based electrolyte that possesses multidentate anions with large

charge delocalization, offering a facile way to prepare Mg electrolytes that achieve reversible Mg deposition. ^{11–13} Despite the significant advancements in the development of the halogen-free, less-corrosive Mg electrolytes, ^{14,15} there is a dire need to establish a fundamental understanding of the chemical and electrochemical processes at the electrolyte/electrode interface. The less-explored interfacial evolution governs the performance and longevity of the Mg battery. Unlike Li-ion battery systems, the electrochemical behavior of the Mg-ion battery system is more complicated largely due to the film formation in a variety of solvents and salts at the Mg

Received: July 20, 2022 Accepted: September 28, 2022 Published: October 7, 2022





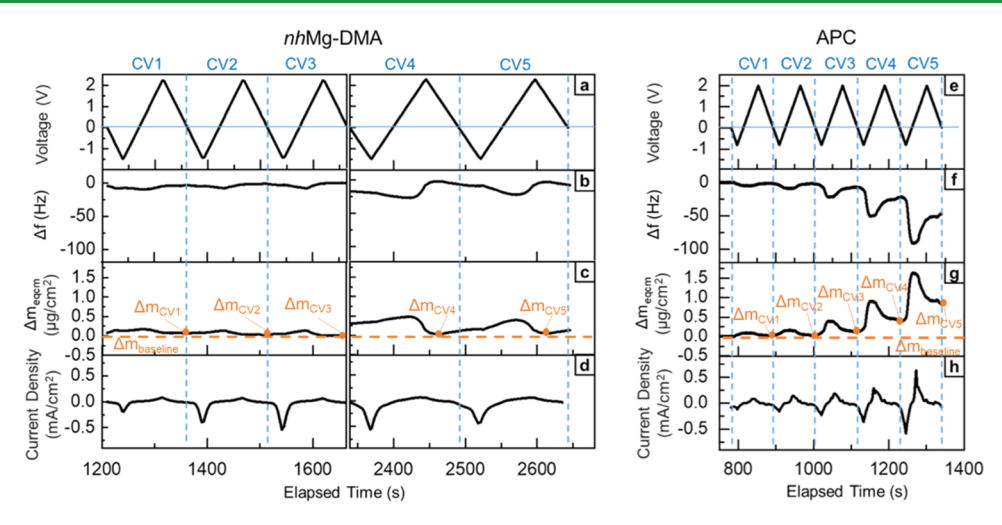


Figure 1. In situ EQCM-D characterization versus electrochemical cycling for a 0.25 M nhMg-DMA electrolyte (a-d) and a 0.2 M APC electrolyte (2PhMgCl + AlCl₃ in THF) (e-h); (a) voltage versus time (CV 1 to 5) for the 0.25 M nhMg-DMA electrolyte. Voltage is scanned from -1.5 to 2.3 V versus Mg²⁺/Mg at a scan rate of 50 mV/s; (b) frequency change (Δf , n = 3) versus time; (c) Sauerbrey mass density change ($\Delta m_{\rm eqcm}$, n = 3) versus time; (d) current density (mA/cm²) versus time; and (e) voltage versus time (CV 1 to 5) for the 0.2 M APC electrolyte. Voltage is scanned from -0.8 to 2.0 V versus Mg²⁺/Mg at a scan rate of 50 mV/s; (f) Frequency change (Δf , n = 3) versus time (n = 3); (g) Sauerbrey mass density change ($\Delta m_{\rm eqcm}$, n = 3) versus time; and (h) current density (mA/cm²) versus time.

metal anode speculated to have a passivation nature. 16 It is also believed that the reactivity of bare Mg metal with trace water, unavoidably present in all nonaqueous electrolytes, promotes the possible formation of magnesium oxide and hydroxide species, which are electrochemically inactive and block further ion transport. 16-19 It has been reported that the MgCl₂/AlCl₃and Mg[B(hexafluoroisopropanol)₄]₂-based electrolytes suffer from a low coulombic efficiency at the initial electrochemical cycles and undergo the electrolyte "conditioning" process, which subsequently promotes reversible Mg deposition.3,12,20-25 Consequently, a series of continuous cyclic voltammogram (CV) scans is required for the conditioning process before reversible Mg plating from MgCl₂/AlCl₃ in THF (tetrahydrofuran) or DME (1,2-dimethoxyethane) electrolytes can be observed. 26-29 However, in the reported electrochemical conditioning process, the SEI formation mechanism and gravimetric changes at the electrolyte/ electrode interface during Mg plating/stripping have not been clarified. Furthermore, questions concerning the progression of the SEI interfacial properties upon short-term or long-term electrochemical cycling remain unanswered.

Merely, a handful of studies reported the electrochemically induced passivation film formation at the Mg electrolyte/electrode interface and its microscopic nature. ^{11,30–33} Involvement of the adsorption-desorption processes and formation of the complexes at the interface during Mg depositiondissolution are extremely complicated and difficult to be studied simply by cyclic voltammetry and $ex\ situ$ analysis methods. The lack of adequate $in\ situ$ techniques is a major roadblock preventing us from understanding the interfacial processes in Mg electrolytes, which are crucial to the development of a practical rechargeable Mg system. Thus, it is critical to provide an in-depth analysis of the interfacial evolution at the Mg metal anode. An important question we aim to answer in this work is whether there is an evolutionary process of the SEI at the Mg interface and what is the dynamic nature of the formed film. Intrigued by the mysteries of the SEI chemistry at the Mg interface, the work presented here offers an in-depth qualitative and quantitative analysis of the SEI

evolution. The in situ SEI formation and its evolution, upon the electrochemical cycles, are investigated with a unique realtime multiharmonic electrochemical quartz crystal microbalance with dissipation (EQCM-D) and probed with electrochemical impedance spectroscopy (EIS), which reveal the complex Mg electrolyte/electrode interface development during the dynamic electrochemical processes. 39-42 Two Mg electrolytes are investigated, the Mg(TFSI)2 electrolyte in tetrahydrofuran (THF) with 2.0 M dimethylamine (DMA) as a cosolvent (referred to as nhMg-DMA) and the all-phenyl complex (APC) electrolyte (phenylmagnesium chloride with aluminum chloride (2:1) in tetrahydrofuran, 2PhMgCl + AlCl₃ in THF). A non-halogen Mg(TFSI)₂ in the DMA-THF system (nhMg-DMA) recently developed by our group offers a novel and simple method to prepare a halogen-free Mg electrolyte that can achieve reversible Mg plating/stripping.¹³ The active component in the nhMg-DMA electrolyte has been proved to be a neutral ion pair structure of Mg²⁺ coordinated with six oxygen atoms (four contributed from the THF molecules, two from the TFSI moieties) located in the first solvation shell, which differs from any other reported halogen-containing Mg electrolytes. 8,13 Mechanisms of how such electrolytes could enable reversible Mg plating and how electrochemical cycling affects the interfacial evolution are not known. In contrast, an APC electrolyte (2PhMgCl + AlCl₃ in THF) is also investigated. The APC electrolyte is considered as the most potential solution that includes organometallic components, for the commercial application of rechargeable Mg batteries. 11,43-45 Although the $(Mg_2(\mu\text{-Cl})_3\cdot 6\text{THF})^+$ cation is verified as the major active intermediate for Mg deposition, 4,46 the SEI evolution on the Mg anode upon electrochemical cycling and how its formation influences ion transport kinetics during electrochemical processes are significantly underreported. Findings in this work present notable differences in the SEI progression in the non-halogen cosolvent-assisted Mg(TFSI)₂ electrolyte versus the halogen-containing APC electrolyte. In the nhMg-DMA electrolyte, the SEI layer undergoes an electrolyte decomposition and reorganization at its initial electrochemical cycles followed by SEI growth in later

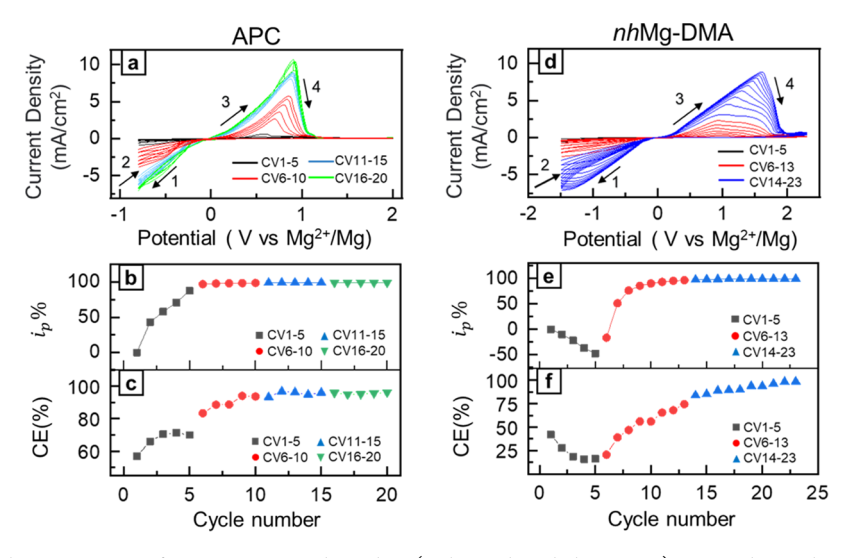


Figure 2. Electrochemical characterizations for a 0.2 M APC electrolyte (2PhMgCl + AlCl₃ in THF) versus electrochemical cycling; (a) continuous cyclic voltammograms of the APC electrolyte for 20 cycles; (b) i_p % versus cycle number; (c) coulombic efficiency versus cycle number; electrochemical characterizations for a 0.25 M nhMg-DMA electrolyte; (d) continuous cyclic voltammograms of the nhMg-DMA electrolyte for 23 cycles; (e) i_p % versus cycle number; and (f) coulombic efficiency versus cycle number; for the CV measurement, the Au-coated resonator is used as the working electrode and Mg metal is used as the counter and reference electrodes; the scan rate is 50 mV/s.

electrochemical cycles that retains a MgF₂-rich interface. However, the APC electrolyte experiences a SEI formation at its initial electrochemical cycles with a subsequent SEI dissolution process upon electrochemical cycling, followed by a stabilization process upon further electrochemical cycling.

RESULTS AND DISCUSSION

SEI Formation and Evolution in the nhMg-DMA and APC Electrolytes. An in situ multiharmonic electrochemical quartz crystal microbalance with dissipation monitoring with a battery flow cell (EQCMD) is devised to assess the formation and evolution of the SEI at the Mg anode/electrolyte interface. A home-built flow cell is used in this measurement with a Aucoated EQCM-D resonator as a working electrode and polished Mg metal as the counter and reference electrodes. Cyclic voltammetry is performed at a scan rate of 50 mV/s, and a series of 20 continuous electrochemical cycles are investigated to evaluate the SEI evolution and its stability. Figure 1 presents the measured frequency shifts (Δf) and the mass density changes $(\Delta m_{\rm eqcm})$ at the interface upon electrochemical cycles for the nhMg-DMA electrolyte (Figure 1a-d) and the APC electrolyte (Figure 1e-h) (electrochemical responses for the later cycles are presented in Figures S1 and S2). Findings suggest a completely different SEI formation development at the initial electrochemical cycles for the nhMg-DMA electrolyte versus the APC electrolyte. A significant irreversible Coulomb loss was observed for the nhMg-DMA electrolyte at its initial CV cycles where the change in current density is disproportional to the frequency shifts. For instance, for a comparable plating current density of −0.5 mA/cm² (3rd cycle) for the *nh*Mg-DMA electrolyte versus the APC electrolyte, a frequency oscillation of merely 8 Hz is observed for the *nh*Mg-DMA electrolyte in contrast with a 22 Hz frequency drop for the APC electrolyte. Consequently, a significant irreversible Coulomb loss for the nhMg-DMA electrolyte is seen (Figure 1b-d) without showing a noticeable frequency drop, and the lost charge is likely contributed to the electrochemical electrolyte reorganization and decomposition processes. On the other hand, the APC electrolyte presents a

layer formation at its initial electrochemical cycles accompanied by a change of the faradaic current proportional to the frequency change, a clear indication of the Mg plating/ stripping that supports the observed mass gain/loss at the interface. Figure 1g presents the mass density changes $(\Delta m_{
m eqcm})$ from the 1st to the 5th electrochemical cycles for the APC electrolyte. The orange-dashed line represents the baseline of the mass density ($\Delta m_{\text{baseline}}$), while the orange circles represent the mass density values after a full electrochemical cycle of Mg plating and stripping $(\Delta m_{cv\#})$. The mass density difference between $\Delta m_{
m cv\#}$ and $\Delta m_{
m baseline}$ represents contributions by the SEI formation. It is worth noting that such a mass density difference is contributed by the mass gain/loss at the interface, which is, in theory, a combination of the SEI mass together with the surface adsorption process. However, the adsorption process mainly results in a monolayer formation at the interface that contributes to a nanogram scale of mass change, and is less than 0.1% of the total layer mass at the microgram scale.⁴⁷ Therefore, the mass density difference between $\Delta m_{cv\#}$ and $\Delta m_{\rm baseline}$ is considered to be exclusively contributed by the SEI process. The SEI layer is continuously growing from the 1st electrochemical cycle to the 5th electrochemical cycle with the Sauerbrey mass density increasing to 1.5 μ g/cm² at the 7th electrochemical cycle.

SEI evolution is further investigated through continuous cyclic voltammetry for the 0.2 M APC electrolyte and the 0.25 M nhMg-DMA electrolyte. Figure 2 presents the current density and coulombic efficiency (CE) versus the continuous electrochemical cycles for the APC electrolyte and the nhMg-DMA electrolyte. For the APC electrolyte, an increase in the anodic and cathodic current densities versus the CV cycle number is primarily observed from CV cycle 1 to 15. However, current density approaches a stable value starting from CV cycle 15 and beyond (Figure 2a,b). The percent increase of the cathodic peak current density (i_p %) is defined as the ratio of the cathodic peak current density of the nth CV cycle ($i_{p,n}$) to the peak current density of the 1st CV cycle ($i_{p,1}$), illustarted in eq. 1

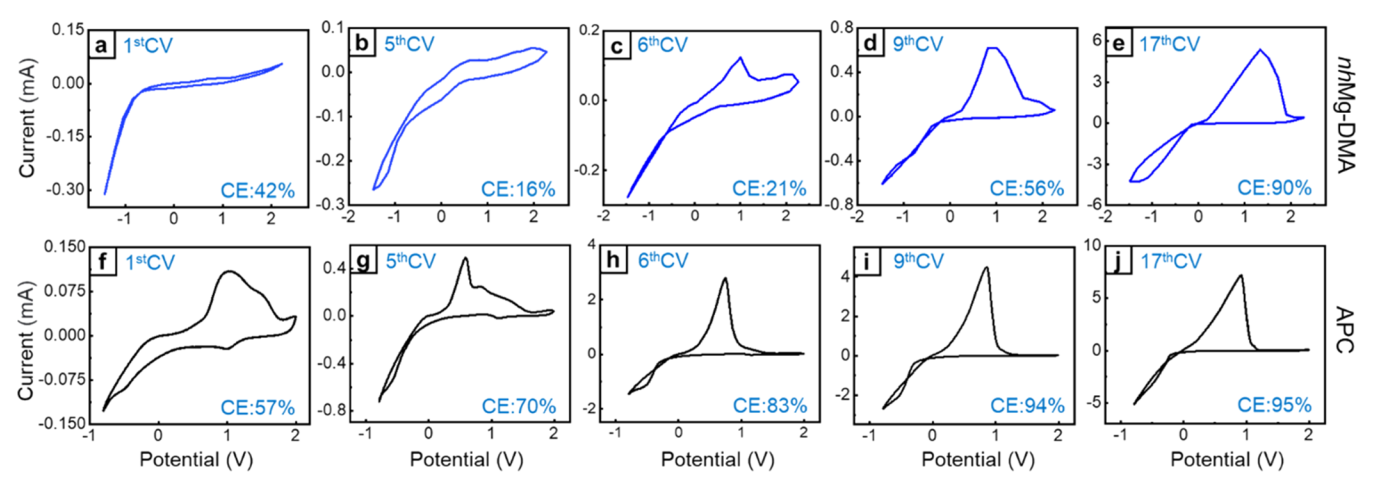


Figure 3. Individual cyclic voltammogram for the 1st, 5th, 6th, 9th, and 17th CV for (a-e) 0.25 M nhMg-DMA electrolyte (blue) and (f-j) 0.2 M APC electrolyte (2PhMgCl + AlCl₃ in THF) (black).

$$i_p\% = \frac{i_{p,n} - i_{p,1}}{i_{p,n}} \times 100\%$$
 (1)

The i_p % is particularly prominent in the early electrochemical cycles for the APC electrolyte. Notably, the trend in i_n % over cycling numbers coincides with the growth of the CE for reversible Mg plating/stripping (Figure 2b,c) in the APC electrolyte. For instance, i_p % (stripping) rapidly increases by a factor of 8 from cycle 1 to 5 and is doubled from cycles 6 to 10, while for further CV cycles, cycle 11 to 15, i_p % show a minor increase of merely 10%. Subsequently, the i_p % reaches a stable value with less than 2% difference after 16 electrochemical cycles evidenced by a near-overlap of the CV graphs. A similar trend is observed for the plating peak current density versus electrochemical cycles (Figure S3). Simultaneously, an improvement of the coulombic efficiency (CE) occurred. For instance, an increase of CE from ~57 to ~70% arises from the electrochemical cycles 1 to 5, followed by a continuous CE increase of an additional 10% from the electrochemical cycle 6 to 10. A less-significant CE increase of merely 2.5% is observed from the electrochemical cycle 11 to 15, and CE is stabilized at 99% at the very last five electrochemical cycles (cycle 16 to 20) for the APC electrolyte (Figure 2c). The simultaneously improved current density and CE for the APC electrolyte at its initial CV cycles (cycle 1 to 5) correspondingly lead to an increase in the Sauerbrey SEI mass density, while the final stabilization of the CE and the current density at further electrochemical cycles concurrently ensues a decrease and stabilization of the Sauerbrery SEI mass density at the interface of the APC electrolyte/electrode.

In contrast, the *nh*Mg-DMA electrolyte presents no apparent reversible Mg plating at its initial five CV cycles. The reversible Mg deposition is not initiated till beyond the 5th electrochemical CV cycle as shown in Figure 3 where individual selected CV cycles are presented for cycle numbers. Substantial irreversible Coulombic consumption is seen at the initial CV cycles for the *nh*Mg-DMA electrolyte without showing a conspicuous film formation at the interface, as evidenced by the minor oscillation of frequency change. The Coulombic loss is attributed to the electrolyte reduction or electrolyte structure reorganization reactions. This observation is significantly different from the APC electrolyte where the evidence of reversible Mg plating and the SEI growth is observed at the initial CV cycles. The increase of the current density along

with the increase of the mass density at the *nh*Mg-DMA electrolyte/electrode interface started to appear at the 6th electrochemical cycle in concert with apparent reversible Mg deposition (Figures 2d—f and 3a—e). A rapid increase of the faradic current of 96.8% that attributes to reversible Mg plating is observed for the *nh*Mg-DMA electrolyte from the 6th to the 13th cycle; subsequently, the faradic current reached a steady state value with less than 3.6% difference after 20 electrochemical cycles. Momentous improvement of the coulombic efficiency is achieved, and CE increased from 16 to 75% from the 6th cycle to the 13th cycle and is finally stabilized at 98% at the very last three electrochemical cycles. On the other hand, the APC electrolyte presented an initial change of CV (cycle 1 to 5) with stabilized CV beyond the 6th electrochemical cycle (Figure 3f—j).

The electrolyte-dependent SEI evolution over electrochemical cycles for the two electrolyte candidates, the *nh*Mg-DMA electrolyte and the APC electrolyte, is summarized in Figure 4. For the *nh*Mg-DMA electrolyte, the SEI mass density is minuscule from CV cycle 1 to cycle 10. However, a negative Sauerbrey mass is observed from electrochemical cycle 12, and

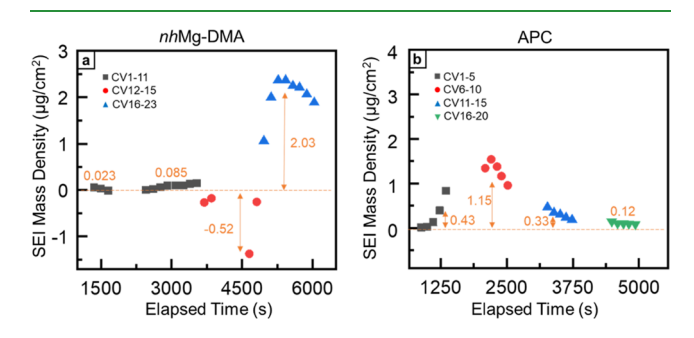


Figure 4. Time-dependent SEI Sauerbrey mass density $\Delta m_{\rm eqcm}$ at the Mg electrolyte/electrode interface; (a) SEI mass density evolution versus time of a 0.25 M nhMg-DMA electrolyte. The color blocks represent different electrochemical cycles, the 1st to the 11th CV (black square), the 12th to the 15th CV (red circle), and the 16th to the 23rd CV (blue triangle); (b) SEI mass density evolution versus time of a 0.2 M APC electrolyte (2PhMgCl + AlCl $_3$ in THF); The color blocks represent different electrochemical cycles, the 1st to the 5th CV (black square), the 6th to the 10th CV (red circle), the 11th to the 15th CV (blue triangle), and the 16th to the 20th CV (green triangle).

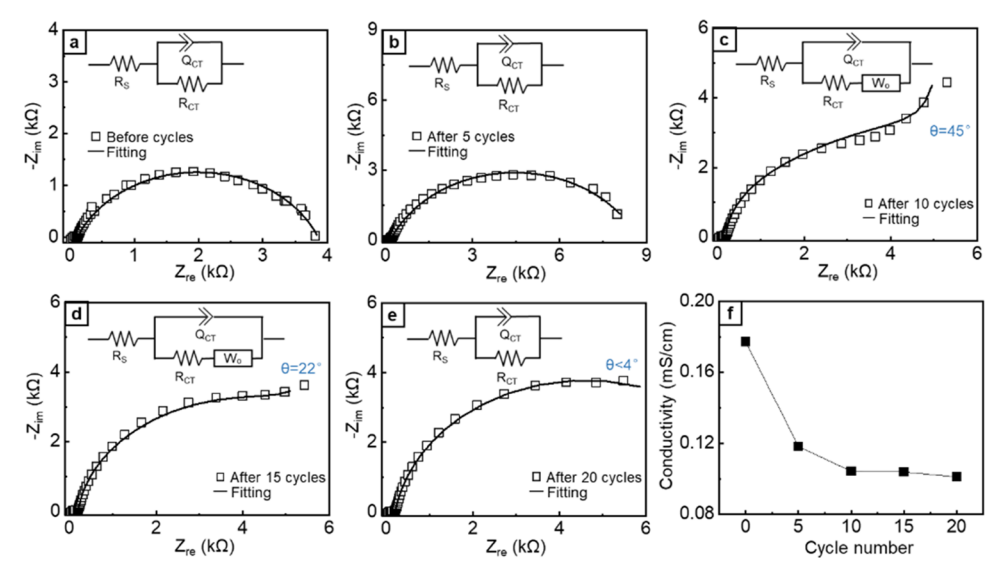


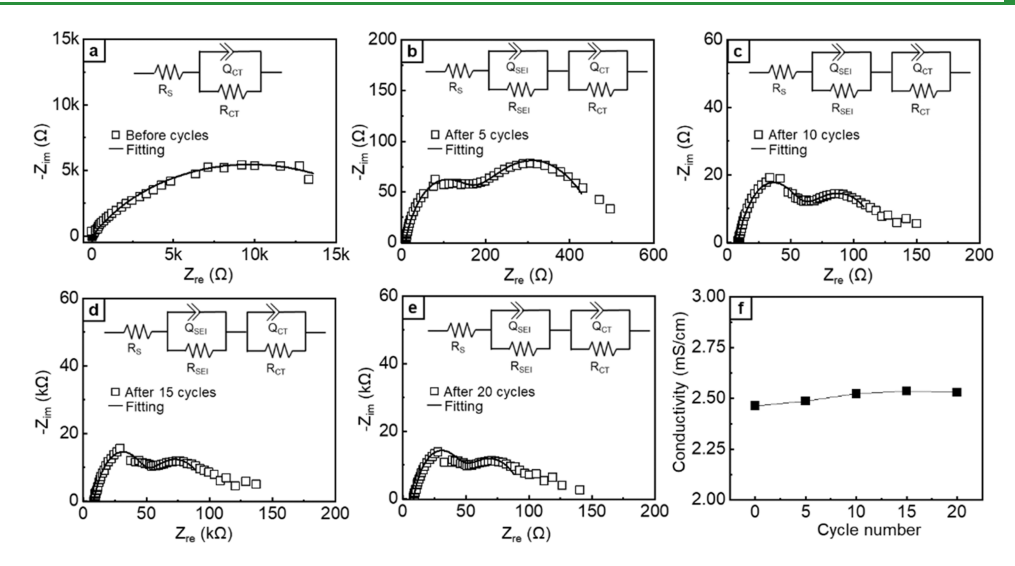
Figure 5. Nyquist plots of a two-electrode Mg cell in a 0.25 M *nh*Mg-DMA electrolyte with fitted equivalent circuits (insets) at (a) 0th, (b) 5th, (c) 10th, (d) 15th, and (e) 20th electrochemical cycles; frequency for the electrochemical impedance spectroscopy (EIS) was from 1 MHz to 0.05 Hz; and (f) conductivity (mS/cm) versus cycle number.

with the continuous CV cycles, the layer mass is finally stabilized at the very last three electrochemical cycles. The negative Sauerbrey mass indicates the contribution from the punctual mass load at the interface, where the Sauerbrey equation for the rigid mass load no longer holds true.⁴⁸ Such an effect is ascribed to a radical-surface reactivity-induced adhered film on the electrode, which can be an indication of the electrolyte reorganization process induced from the lost charge. 34,49,50 For the APC electrolyte, the SEI mass density gives a monotonic growth over the first 7 CV cycles; however, the SEI mass density starts to decrease from the 7th CV cycle to the 15th CV cycle, which is a representative trend of the SEI dissolution process. Afterward, a stabilization of the SEI is seen, which indicates a stable Mg electrolyte/electrode interface. These findings indicate the SEI growth, dissolution, and stabilization progression for the APC electrolyte along the electrochemical stimulations from cycling.

In Situ EIS Analysis for the nhMg-DMA and APC Electrolytes. The *in situ* electrochemical characterization coupled with the EQCM-D measurements suggests different SEI evolutions upon electrochemical cycles for a non-halogen Mg(TFSI)₂ electrolyte (*nh*Mg-DMA electrolyte) and a halogen-containing APC electrolyte. The findings stimulate further interfacial characterization to investigate the time-dependent SEI evolution. Herein, the EIS analysis is performed in real time to probe the time-dependent electrochemical cycling-induced change at the interface.

The electronic element parameters electrolyte resistance $(R_{\rm s})$, charge transfer resistance $(R_{\rm ct})$, double-layer capacitance $(Q_{\rm ct})$, and Warburg impedance $(W_{\rm o})$ in the equivalent circuit models were fitted using Aftermath software to be closely consistent with the experimentally measured EIS for the *nh*Mg-DMA electrolyte (Figure 5). Before electrochemical cycling, shown in Figure 5a, the EIS spectrum shows a depressed semicircle response with the nonlinear portion presented in a low-frequency region $(0.05-1~{\rm Hz})$. The fitted curve presents one interface development, giving the charge transfer resistance $R_{\rm ct}=3.5~{\rm k}\Omega$ in parallel with a double-layer capacitance of $Q_{\rm ct}=129~\mu{\rm F}$. The large double-layer capacitance of 129 $\mu{\rm F}$ suggests a strong electrolyte—electrode adsorption process. After five

continuous electrochemical cycles (Figure 5b), the size of the semicircle increases with decreasing ion diffusion rate. Specifically, an increased $R_{\rm ct}$ of 8.6 k Ω is observed as compared with R_{ct} before electrochemistry (3.5 k Ω), an indication of reduced ion transport kinetics or the required energy barrier for cation desolvation. Simultaneously, the extent of Q_{ct} is declined from 129 to 45 μ F, suggesting a reconstruction of the electrolyte structure adjacent to the electrode. After 10 continuous electrochemical cycles (Figure 5c), the EIS spectrum changed from a defined semicircle to a deformed shape with a contracted diameter in the high- to medium-frequency range, which is in connection with a characteristic 45° slope line at the low-frequency range (<0.1 Hz), representing the Warburg impedance (W_0) . In this case, a conductive SEI with improved charge transfer kinetics is formed, as evidenced by a decrease of R_{ct} from 8.6 to 3.1 k Ω . More importantly, the appearance of the Warburg diffusion component ($W_0 = 3.2 \text{ k}\Omega \cdot \text{s}^{-1/2}$) indicates a kinetically facile mass transfer process ascribed to the ion diffusion from the electrolyte through the as-formed SEI layer, which starts to play a role. This finding is in good agreement with the EQCMD results, where an increased mass density starts to appear beyond the 10th electrochemical cycle. After the 10th electrochemical cycle (Figure 5c,d), the EIS spectrum suggests a coexistence of charge transfer and mass transfer processes with two constant phase element (CPE) components seen. After the 15th electrochemical cycle, an increased R_{ct} to 5.7 $k\Omega$, Q_{ct} from 86 to 163 μF, and a decreased W_{o} to 1.6 $k\Omega \cdot s^{-1/2}$ with 22° slope angle are observed. Such changes suggest a complicated interfacial revolution process with a slowed transfer kinetics for a heterogeneous process at the interface.⁴⁷ After the 20th electrochemical cycle (Figure 5e), R_{ct} continuously increases to 8.8 k Ω and Q_{ct} is increased from 163 to 230 μ F with the disappearance of the Warburg diffusion component, suggesting a decreased ion transport through the formed SEI layer with a possibly increased layer resistance. The increase of Qct is possibly attributed to the desolved ions trapped at the interface, resulting in the built-up charge separation, which is mostly a heterogeneous process and eventually leads to a decreased charge transfer kinetics.



www.acsami.org

Figure 6. Nyquist plots of a two-electrode Mg cell in a 0.2 M APC electrolyte with the fitted equivalent circuit (inset) at the 0th (a), 5th (b), 10th (c), 15th (d), and 20th (e) electrochemical cycles; frequency for the electrochemical impedance spectroscopy (EIS) was from 1 MHz to 0.05 Hz; and (f) conductivity (mS/cm) versus cycle number.

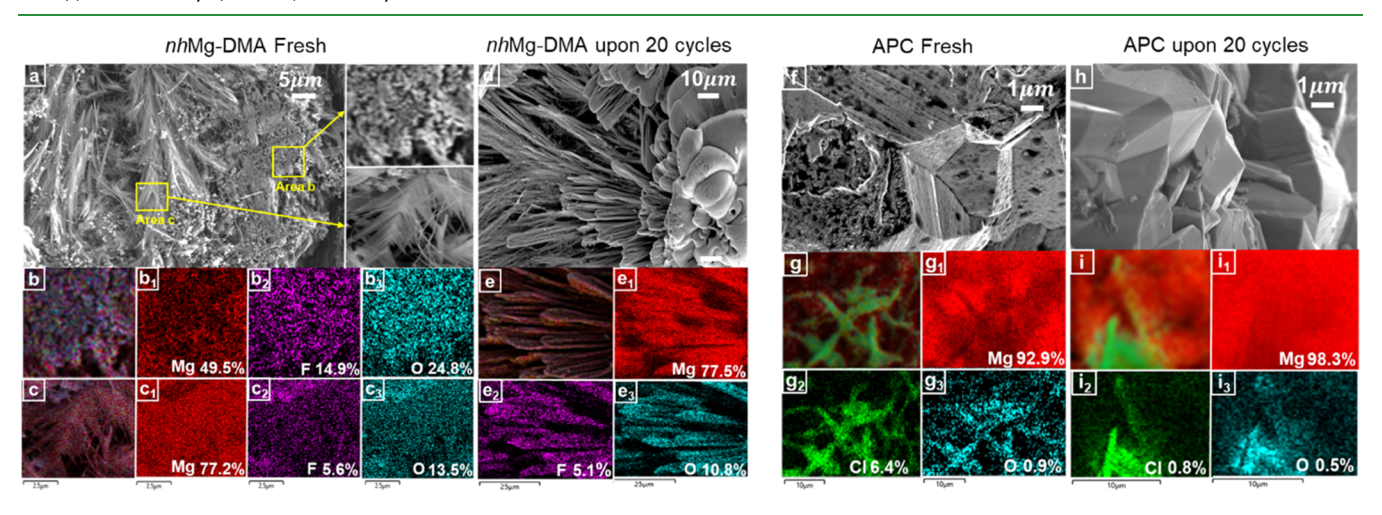


Figure 7. FESEM images and EDS mapping of the electrochemically deposited Mg^0 from: (a-c) freshly prepared 0.25 M nhMg-DMA electrolyte; $b_1 \cdot b_3$ and $c_1 \cdot c_3$ represent elemental mapping for Mg (red), F (purple), and O (blue), respectively; (d-e) nhMg-DMA electrolyte after 20 electrochemical cycles; $e_1 - e_3$ represent elemental mapping for Mg (red), F (purple), O(blue); (f-g) freshly prepared 0.2 M APC electrolyte; $g_1 \cdot g_3$ represent elemental mapping for Mg (red), Cl (green), and O (blue); and (h-i) APC electrolyte after 20 electrochemical cycles; $i_1 - i_3$ represent elemental mapping for Mg (red), Cl (green), and O (blue), respectively.

The electronic elements R_{sv} R_{ctv} R_{SELv} Q_{ctv} and Q_{SEI} in the equivalent circuit models were fitted using Aftermath software, closely consistent with the experimentally measured EIS spectrum for the APC electrolyte (Figure 6). In the fitted circuits, $R_{s_i}R_{ct}$ R_{SEI} Q_{ct} and Q_{SEI} represent the electrolyte resistance, charge transfer resistance, SEI resistance, doublelayer capacitance, and the capacitance contributed from the SEI. Before the electrochemical cycling, shown in Figure 6a, the EIS spectra give a depressed semicircle response with the nonlinear portion of EIS shown in the low-frequency region (<1 Hz), corresponding to the charge transfer resistance (R_{ct} = 19 k Ω) in parallel with the double-layer capacitance ($Q_{ct} = 57$ μ F). The appearance of the large impedance of R_{ct} = 19 k Ω before the start of the electrochemical cycling could potentially account for the initial surface adsorption in the APC electrolyte, which leads to a high charge transfer resistance across the interface, while the Q_{ct} of 57 μF represents the charge separation due to the nonspecific adsorbed ionic species at the interface. After five continuous electrochemical cycles (Figure 6b), an interfacial evolution with SEI formation is clearly observed, resulting in the appearance of two semicircles in the EIS spectrum. The 1st semicircle appears at the midhigh-frequency regime from 1000 to 100 Hz, which gives $R_{\rm SEI}$ = 141 Ω and $Q_{\rm SEI}$ = 49 μ F. The 2nd semicircle represents the interface related to the charge transfer process that is presented at the low-frequency regime from 1 Hz to 0.05 Hz, with R_{ct} = 335 Ω and Q_{ct} = 1543 μ F. Results suggest a drastically lowered $R_{\rm ct}$ (from 19 k Ω to 335 Ω) upon initial electrochemical cycling, and such a resistance drop suggests the critical role of the electrochemical process, which regenerates the interface that possibly removes the surface adsorption followed by the formation of a conductive SEI. The R_{ct} values continuously decrease to 70 Ω after the 10th electrochemical cycle, followed by reaching a stable value of around 54 Ω at the 15th and 20th cycles (Figure 6c-e). The perpetually decreased R_{ct} upon electrochemical cyclings reveals an enhancement of the ion transport kinetics. The $R_{\rm SEI}$ presents a similar evolution upon electrochemical cycling, where $R_{\rm SEI}$ is decreased from 141 Ω

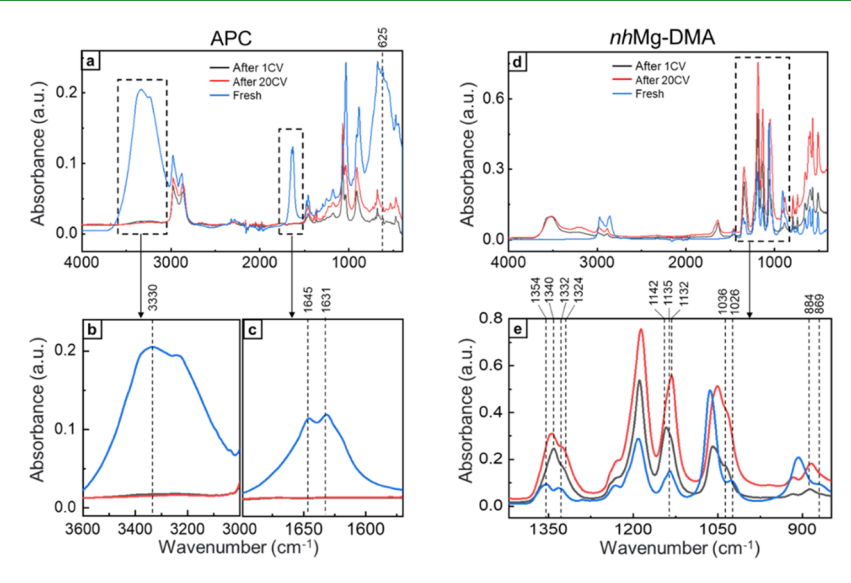


Figure 8. FTIR spectra of (a) as-prepared 0.2 M APC electrolyte (blue). Electrolyte after one (black) and 20 (red) electrochemical cycles; (b-c) zoomed-in spectra of (a); and (d) as-prepared 0.25 M nhMg-DMA electrolyte (blue). Electrolyte after one (black) and 20 (red) electrochemical cycles and (e) zoomed spectra of (d).

(at the 5th CV) to 46 Ω (at the 10th cycle), followed by stabilization at the 15th CV and the 20th CV, resulting in $R_{\rm SEI}$ values of 38 and 36 Ω , respectively. Such findings suggest that the continuous electrochemical cycling ultimately enables a facile charge transfer kinetics, which indicates the formation of a more conductive SEI at the interface. More importantly, the evolution of the SEI and the improvement of its conductivity are electrochemical cycle number-dependent, which represents interesting SEI dynamics. Measurements from EIS are in good agreement with the EQCM-D findings, where an initial gain of the SEI mass density is seen at early cycles followed by a decrease in mass density and finally a stabilization process at the interface at further electrochemical cycles.

Evolution of the electrolyte conductivity that reflects the type and number of the coordinated and decoordinated molecules to the Mg metal center versus electrochemical cycling for the nhMg-DMA and APC electrolytes is presented in Figures 5f and 6f, respectively. For the APC electrolyte, electrolyte conductivity stays unaffected by the electrochemical cycling with $\sigma = 2.5$ mS/cm. This outcome indicates that the ionic species in solution remains unperturbed by the electrochemical cycling, while the SEI growth is controlled by the electrochemical signals. Interestingly, for the nhMg-DMA electrolyte, electrolyte conductivity is decreased from 0.18 to 0.1 mS/cm after 10 CV cycles, and this observation happens together with the loss of Coulomb and the increase of the mass density at the interface probed by EQCM-D. Such a change of the electrolyte conductivity could be ascribed to the exchange of the solvent molecules from the Mg solvation shell that is directly accountable for making or breaking the ionic structures, which consequently affects the conductivity. At further electrochemical cycles, electrolyte conductivity stays at a constant value of 0.1 mS/cm, an indication of a more stable electrolyte configuration, thus resulting in the exchange of the TFSI coordination in agreement with the reported pair distribution function analysis.¹³

FESEM/EDS Characterization and FTIR Analysis. The electrochemically instigated SEI evolution mechanisms for the nhMg-DMA and APC electrolytes are further investigated with ex situ FESEM/EDS and FTIR analysis to reveal the chemical

and morphological information at the interface. For the nhMg-DMA electrolyte (Figure 7a-e), a better organized and more uniform Mg⁰ deposition morphology is seen for the cycled electrolyte in contrast to that of the freshly prepared electrolyte. Electrochemically deposited Mg⁰ from a freshly prepared nhMg-DMA electrolyte gives two different structures under FESEM, the Mg-rich region with ~77% Mg (area c) and the Mg-poor region with \sim 50% of Mg (area b). The chemical composition and distribution for these two areas are completely different where the Mg-poor region contained a higher percentage of F (14.9%) and O (24.8%) as compared to a lower percentage of F (5.6%) and O (13.5%) in the Mg-rich region. This finding indicates that an electrolyte-evolved surface chemical reaction happened before Mg deposition. On the other hand, the electrochemically cycled nhMg-DMA presents a homogeneous morphology with the deposited Mg⁰ with a larger grain size that is instigated by the decline of the polycrystallization process, which consequently reduces the Mg nucleation sites.

Figure 7f-i presents the FESEM and the energy-dispersive X-ray spectroscopy (EDS) analysis for the 0.2 M APC electrolyte, where the deposited Mg⁰ morphology can be seen from both the freshly prepared APC electrolyte (Figure 7f) and the cycled APC electrolyte (Figure 7h). For the APC electrolyte, the morphology of the electrochemically cycled APC gives a smooth surface as compared to that of the electrochemically deposited Mg⁰ from the freshly prepared APC with obvious corrosion sites. The 2D EDS mapping presents an improved Mg⁰ deposition with less impurities after 20 electrochemical cycles as compared with the as-made electrolyte, as evidenced by an improvement of the Mg⁰ composition, from 93 to 98% and a decrease of the Cl and O signals (6.4-0.8% for Cl, 0.9-0.5% for O). The improved Mg⁰ purity and a smooth Mg⁰ morphology prove a chloridefree and cleaner Mg⁰ metal deposition that is facilitated through the electrochemical cycling for APC. Comparing the above-mentioned results for the nhMg-DMA and APC electrolytes, a MgF2-rich layer is seen for the electrochemically deposited Mg⁰ from the nhMg-DMA electrolyte, while no

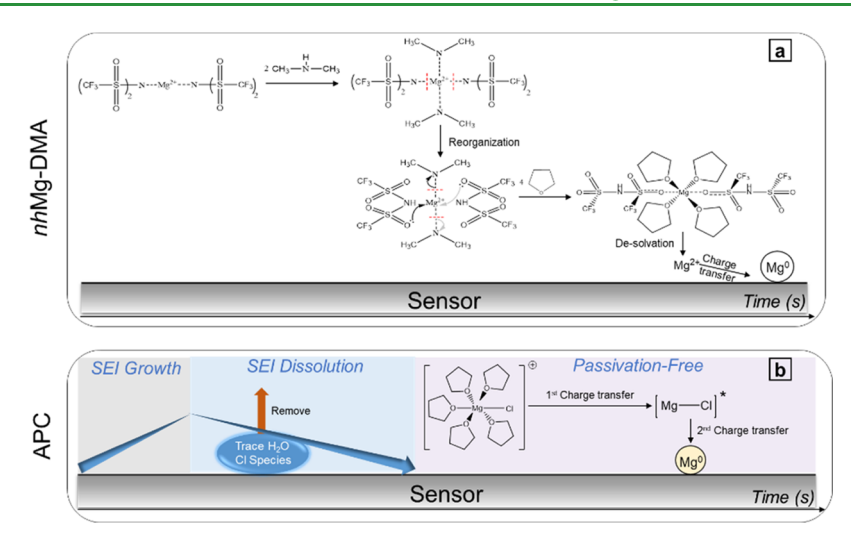


Figure 9. Proposed SEI evolution mechanisms at the electrolyte/electrode interface upon electrochemical cycling for (a) nhMg-DMA electrolyte and (b) APC electrolyte.

compelling surface layer is seen for the electrochemically cycled APC electrolyte.

For the FTIR analysis, three different electrochemical conditions were investigated: electrolytes after one electrochemical cycle, electrolytes upon 20 electrochemical cycles, and freshly prepared electrolytes. FTIR results are presented in Figure 8. The APC electrolyte mostly retained its spectral features upon electrochemical cycling with the exception of the disappearance of the 3330 cm⁻¹ O-H stretching and the 1645 and 1631 cm⁻¹ H-O-H bending vibrations as compared to the freshly prepared APC (Figure 8a-c).⁵¹ The loss of the H-O-H bending and the O-H stretching suggests the electrolysis reactions triggered by the electrochemical cycling that resulted in water decomposition. In addition, the disappearance of the 625 cm⁻¹ peak after electrochemical cycling is assigned to the torsion mode of C-O-C-C in tetrahydrofuran, indicating association of the THF molecule with the Mg center upon cycling.⁵² On the other hand, FTIR of the nhMg-DMA electrolyte showed greater variations under different electrochemical conditions (Figure 8d,e).53 Results for the electrochemically cycled nhMg-DMA electrolyte presented three pieces of signature evidence representing reorganization of the Mg(TFSI)₂ coordination structure, with the most significant change occurring at the asymmetric stretching of the ν_{as} O=S=O, which occurred at 1354 cm⁻¹ for the freshly prepared nhMg-DMA electrolyte,54 but this peak shifted to ~1340 cm⁻¹ after electrochemical cycling. This finding suggests the formation of the weak coordination of the Mg···O₂SCF₃, which replaced the coordinated structure of the Mg···NSO₂CF₃. Another major difference in the FTIR appeared at the signature CF3-SO2-N···Mg vibration from the TFSI⁻ at 1332 cm⁻¹ being shifted to 1324 cm⁻¹ upon electrochemical cycling.⁵⁴ This finding indicates possible detachment of the Mg coordination from TFSI- and the formation of the CF₃-SO₂-N···H environment. This electrolyte reorganization is further confirmed by the shift of the signature symmetric TFSI···Mg coordination from 1135 to 1142 cm⁻¹ and 1132 cm⁻¹ at the 1st and 20th electrochemical cycles, respectively. Consequently, a new coordination sphere of Mg with four oxygen atoms from THF and two oxygen atoms from TFSI is formed; deformation of the THF structure further confirms the new coordination environment

of the Mg center upon electrochemical cyclings. For instance, the symmetric ν_s C-O-C stretching from THF at 869 cm⁻¹ is blue-shifted to 884 cm⁻¹ after electrochemical cycles, suggesting deformation of the THF solvent molecules. 55 This finding also agrees with the blue shift of the 1026 cm⁻¹ peak to 1036 cm⁻¹, an indication of the THF ring structure deformation ascribed to the steric hindrance from the progression of SO_2 -N- to the Mg center. SS

In accordance with the above-mentioned findings, the proposed mechanism for the Mg(TFSI)₂ structural evolution upon electrochemical cycling is shown in Figure 9a, where a large Coulombic loss is seen at the early electrochemical cycles without a noticeable SEI formation, but a large charge transfer resistance is observed. A reorganization of the coordination environment of the Mg center occurred upon electrochemical cycling, and continuous electrochemical cycles enable reversible Mg deposition with improved CE and retain a MgF2-rich SEI layer structure. The proposed mechanism of the SEI evolution for the APC electrolyte is presented in Figure 9b, where SEI formation is initiated at early electrochemical cycles. Continuous electrochemical cycles enable a SEI dissolution process accompanied by the improved CE with water and chloride removed, leading to a stabilized SEI at further electrochemical cycles with enhanced charge transport kinetics.

CONCLUSIONS

SEI formation and evolution at the Mg electrolyte/electrode interface are systematically examined upon electrochemical stimulations in two interesting Mg electrolytes, a non-halogencontaining nhMg-DMA electrolyte and a halogen-containing APC electrolyte. Results from the in situ EQCM-D coupled with EIS measurements, electrochemical characterization, FTIR, FESEM, and EDS analysis offer multifold evidence to elucidate the dynamic SEI evolution. For the APC electrolyte, there is an initial SEI formation followed by the subsequent stabilization of the SEI, where an improved CE is observed upon continuous electrochemical cycling. This ultimately leads to a better refined and organized electrochemically deposited Mg⁰ morphology. On the other hand, the nhMg-DMA electrolyte went through the electrolyte reconstruction process, resulting in a significant Couloumbic loss evidenced by a disproportional charge loss from the mass density change

through the EQCM-D measurements and formation of a new coordination sphere with Mg, as evidenced by the FTIR results. Continuous electrochemical cycling enables reorganization of the electrolyte structure, which ultimately benefits the charge transfer kinetics in the nhMg-DMA electrolyte with improved reversible Mg plating. The work reported here utilizes an innovative in situ electroanalytical technique to explore SEI evolution at the Mg electrolyte/electrode interface upon electrochemical cycling. The dynamic interfacial layer formation and evolution at the Mg electrolyte/electrode upon continuous electrochemical stimulation are essential to investigate, and results from this report offer potential guidelines to design a stable interface for secondary Mg energy storage devices.

EXPERIMENTAL SECTION

Electrolyte Preparation. All electrolytes were prepared in an argon-filled glovebox (Vacuum Technology Inc.) with H₂O and O₂ levels under 1.0 ppm. Magnesium (II) bis(trifluoromethanesulfonyl)imide (99.5%, Solvionic) was dried overnight (at 180 °C, <100 mTorr) in a vacuum oven (Glass Oven B-585, BUCHI Corp.) before use. Dimethylamine (99.5%, anhydrous, Acros Organics) and tetrahydrofuran (99.5%, anhydrous, Sigma Aldrich) solvents were pretreated with dried molecular sieves (Aldrich, 3 Å Beads, 4-8 mesh) for 24 h before preparing the electrolyte. Preparation of 0.25 M Mg(TFSI)₂ in THF with a 2.0 M DMA cosolvent (nhMg-DMA electrolyte) was reproduced from recent work from our group. 12 Phenylmagnesium chloride (99.5%, Sigma Aldrich), aluminum chloride (99.9%, Sigma Aldrich), and THF (99.5%, anhydrous, Sigma Aldrich) were used to prepare a 0.2 M APC electrolyte (2PhMgCl + AlCl $_3$ in THF) in accordance with the reported literature. 31,43

Electrochemical Measurements. A home-designed in situ electrochemical cell was coupled with an electrochemical quartz crystal microbalance instrument (Q-Sense, Biolin Scientific Inc.). The electrochemical measurements were performed in an argon-filled glovebox with H₂O and O₂ levels under 1.0 ppm. An AT-cut 5 MHz quartz crystal resonator (Biolin Scientific Inc.) was used as the working electrode, and polished magnesium metal (99.9% purity, Sigma-Aldrich) served as the reference and counter electrodes for the electrochemical experiments. A Kalrez O-ring (Biolin Scientific) was placed between the quartz resonator and the Mg metal electrode, leaving an exposed geometric area of 0.785 cm² of the quartz resonator in contact with the electrolyte. Before introducing the electrolyte into the electrochemical cell, the quartz resonator was stabilized in air and the baseline frequency and dissipation curves were recorded. Multiharmonic EQCM-D measurements were obtained at odd overtones (n = 3, 5, 7, 9, 11, 13). Data acquisition for the EQCM-D measurements was performed using QSoft401 software (Biolin Scientific Inc.). Electrochemical impedance spectroscopy (EIS) was applied at the frequency range from 0.05 Hz to 1 MHz with an amplitude of 5 mV for a two-electrode Mg cell (working electrode area = 0.97 cm²). For the 0.25 M Mg (TFSI)₂ in DMA-THF (nhMg-DMA) electrolyte, the electrochemical measurements were carried out for a total of 20 electrochemical cycles with the in situ EIS probed under a DC voltage of 0.02 V (versus Mg) at the 0th, 5th, 10th, 15th, and 20th cycles. For the 0.2 M APC (2PhMgCl + AlCl₃ in THF) electrolyte, the electrochemical measurements were carried out for 20 electrochemical cycles with the in situ EIS probed under a DC voltage of 0.02 V (versus Mg) at the 0th, 5th, 10th, 15th, and 20th cycles. Data from the electrochemical measurements were collected through VersaStudio.

FTIR Analysis. The ATR-FTIR spectra were acquired using a Nicolet iS50 Fourier transform infrared spectrometer (FTIR) equipped with an attenuated total reflectance (ATR) module. FTIR spectral data were collected by performing 32 scans with a spectral resolution of 4 cm⁻¹ in the range between 4000 and 400 cm⁻¹. The platinum electrode is used as a working electrode, and polished

magnesium metal is applied as reference and counter electrodes. The electrolytes were prepared and electrochemically cycled in an argonfilled glovebox. The as-prepared electrolytes, electrolytes after one electrochemically cycle, and electrolytes after 20 consecutive electrochemical cycles were immediately transferred on to the ATR stage located outside the glovebox for FTIR characterization. Electrochemical cycling was performed in the potential window from -0.8 to 2.0 V for the APC electrolyte (scan rate 50 mV/s) and from -1.5 to 2.3 V for the nhMg-DMA electrolyte (scan rate 50 mV/s). Data acquisition and spectral calculations were performed using OMNIC

Field Emission Scanning Electron Microscopy (FESEM) and Energy-Dispersive X-Ray Spectroscopy (EDS). Samples for FESEM imaging were prepared by electrochemically plating Mg metal in the 3-electrode cell with Pt as a working electrode (2.0 mm diameter) and polished Mg metal as reference and counter electrodes. The Pt working electrode was polished to a mirror finish with alumina powder (0.05 μ m) solution. All electrolyte preparation and electrodeposition were carried out under an inert atmosphere in an Ar-filled glovebox (H₂O and O₂ under 1 ppm). The Mg deposition was obtained using chronopotentiometry at -0.30 mA/cm^2 for 12 h. The obtained Mg deposits were rinsed with DMC and held under vacuum for 2 h for drying before imaging. Microstructure characterization was performed via scanning electron microscopy (Sigma500 VP FESEM, Zeiss). The elemental mappings were performed with an energydispersive spectrometer (EDS, Oxford Instruments) mounted on the FESEM with the data analysis performed using the Aztec software package.

ASSOCIATED CONTENT

Supporting Information

The Supporting Information is available free of charge at https://pubs.acs.org/doi/10.1021/acsami.2c13037.

Additional electrochemical characterizations results and EDS and EQCM-D data (PDF)

AUTHOR INFORMATION

Corresponding Author

Niya Sa - Department of Chemistry, University of Massachusetts Boston, Boston, Massachusetts 02125, United States; o orcid.org/0000-0003-4656-5851; Email: Niya.Sa@umb.edu

Authors

Shengqi Fan – Department of Chemistry, University of Massachusetts Boston, Boston, Massachusetts 02125, United

Saida Cora – Department of Chemistry, University of Massachusetts Boston, Boston, Massachusetts 02125, United

Complete contact information is available at: https://pubs.acs.org/10.1021/acsami.2c13037

Author Contributions

S.F. performed the experimental data collections and data analysis; S.C. helped with the FESEM/EDS data collection and article preparation; N.S. led the project, data organization, and article writing with inputs from all listed authors. All authors have given an approval to the final version of the article.

The authors declare no competing financial interest.

ACKNOWLEDGMENTS

This work is financially supported by the National Science Foundation CAREER grant (no. 2047753). Acquisition of the FESEM and EDS data is supported by the advanced FESEM by the NSF MRI grant (no. 1919919). Research development grant from the University of Massachusetts Boston is acknowledged.

REFERENCES

- (1) Muldoon, J.; Bucur, C. B.; Gregory, T. Quest for Nonaqueous Multivalent Secondary Batteries: Magnesium and Beyond. *Chem. Rev.* **2014**, *114*, 11683–11720.
- (2) Deivanayagam, R.; Ingram, B. J.; Shahbazian-Yassar, R. Progress in Development of Electrolytes for Magnesium Batteries. *Energy Storage Mater.* **2019**, *21*, 136–153.
- (3) Doe, R. E.; Han, R.; Hwang, J.; Gmitter, A. J.; Shterenberg, I.; Yoo, H. D.; Pour, N.; Aurbach, D. Novel, Electrolyte Solutions Comprising Fully Inorganic Salts with High Anodic Stability for Rechargeable Magnesium Batteries. *Chem. Commun.* **2014**, *50*, 243–245.
- (4) Yoo, H. D.; Shterenberg, I.; Gofer, Y.; Gershinsky, G.; Pour, N.; Aurbach, D. Mg Rechargeable Batteries: An On-Going Challenge. *Energy Environ. Sci.* **2013**, *6*, 2265–2279.
- (5) Aurbach, D.; Lu, Z.; Schechter, A.; Gofer, Y.; Gizbar, H.; Turgeman, R.; Cohen, Y.; Moshkovich, M.; Levi, E. Prototype Systems for Rechargeable Magnesium Batteries. *Nature* **2000**, 407, 724–727.
- (6) Mohtadi, R.; Mizuno, F. Magnesium batteries: Current State of the Art, Issues and Future Perspectives. *Beilstein J. Nanotechnol.* **2014**, *5*, 1291–1311.
- (7) Fan, S.; Asselin, G. M.; Pan, B.; Wang, H.; Ren, Y.; Vaughey, J. T.; Sa, N. A Simple Halogen-Free Magnesium Electrolyte for Reversible Magnesium Deposition through Cosolvent Assistance. *ACS Appl. Mater. Interfaces* **2020**, *12*, 10252–10260.
- (8) Ha, S. Y.; Lee, Y. W.; Woo, S. W.; Koo, B.; Kim, J. S.; Cho, J.; Lee, K. T.; Choi, N. S. Magnesium(II) Bis(trifluoromethane sulfonyl) Imide-Based Electrolytes with Wide Electrochemical Windows for Rechargeable Magnesium Batteries. *ACS Appl. Mater. Interfaces* **2014**, *6*, 4063–4073.
- (9) Tutusaus, O.; Mohtadi, R.; Arthur, T. S.; Mizuno, F.; Nelson, E. G.; Sevryugina, Y. V. An Efficient Halogen-Free Electrolyte for Use in Rechargeable Magnesium Batteries. *Angew. Chem., Int. Ed.* **2015**, *54*, 7900–7904.
- (10) Carter, T. J.; Mohtadi, R.; Arthur, T. S.; Mizuno, F.; Zhang, R. G.; Shirai, S.; Kampf, J. W. Boron Clusters as Highly Stable Magnesium-Battery Electrolytes. *Angew. Chem., Int. Ed.* **2014**, *53*, 3173–3177
- (11) Attias, R.; Salama, M.; Hirsch, B.; Goffer, Y.; Aurbach, D. Anode-Electrolyte Interfaces in Secondary Magnesium Batteries. *Joule* **2019**, *3*, 27–52.
- (12) Shterenberg, I.; Salama, M.; Yoo, H. D.; Gofer, Y.; Park, J. B.; Sun, Y. K.; Aurbach, D. Evaluation of (CF3SO2)(2)N- (TFSI) Based Electrolyte Solutions for Mg Batteries. *J. Electrochem. Soc.* **2015**, *162*, A7118—A7128.
- (13) Fan, S. Q.; Asselin, G. M.; Pan, B. F.; Wang, H.; Ren, Y.; Vaughey, J. T.; Sa, N. Y. A Simple Halogen-Free Magnesium Electrolyte for Reversible Magnesium Deposition through Cosolvent Assistance. ACS Appl. Mater. Interfaces 2020, 12, 10252–10260.
- (14) Mandai, T.; Tatesaka, K.; Soh, K.; Masu, H.; Choudhary, A.; Tateyama, Y.; Ise, R.; Imai, H.; Takeguchi, T.; Kanamura, K. Modifications in Coordination Structure of Mg[TFSA](2)-Based Supporting Salts for High-Voltage Magnesium Rechargeable Batteries. *Phys. Chem. Chem. Phys.* **2019**, 21, 12100–12111.
- (15) Sheha, E.; Farrag, M.; Fan, S. Q.; Kamar, E.; Sa, N. Y. A Simple Cl⁻ Free Electrolyte Based on Magnesium Nitrate for Magnesium-Sulfur Battery Applications. *ACS Appl. Energy Mater.* **2022**, *5*, 2260–2269.
- (16) Aurbach, D.; Gofer, Y.; Schechter, A.; Chusid, O.; Gizbar, H.; Cohen, Y.; Moshkovich, M.; Turgeman, R. A Comparison between the Electrochemical Behavior of Reversible Magnesium and Lithium Electrodes. *J. Power Sources* **2001**, *97*–*98*, 269–273.

- (17) Aurbach, D.; Gofer, Y.; Lu, Z.; Schechter, A.; Chusid, O.; Gizbar, H.; Cohen, Y.; Ashkenazi, V.; Moshkovich, M.; Turgeman, R.; Levi, E. A Short Review on the Comparison between Li Battery Systems and Rechargeable Magnesium Battery Technology. *J. Power Sources* **2001**, 97–98, 28–32.
- (18) Lu, Z.; Schechter, A.; Moshkovich, M.; Aurbach, D. On the Electrochemical Behavior of Magnesium Electrodes in Polar Aprotic Electrolyte Solutions. *J. Electroanal. Chem.* **1999**, 466, 203–217.
- (19) Connell, J. G.; Genorio, B.; Lopes, P. P.; Strmcnik, D.; Stamenkovic, V. R.; Markovic, N. M. Tuning the Reversibility of Mg Anodes via Controlled Surface Passivation by H2O/Cl⁻ in Organic Electrolytes. *Chem. Mater.* **2016**, 28, 8268–8277.
- (20) He, S. J.; Luo, J.; Liu, T. L. MgCl2/AlCl3 Electrolytes for Reversible Mg Deposition/Stripping: Electrochemical Conditioning or Not? *J. Mater. Chem. A* **2017**, *5*, 12718–12722.
- (21) Dlugatch, B.; Mohankumar, M.; Attias, R.; Krishna, B. M.; Elias, Y.; Gofer, Y.; Zitoun, D.; Aurbach, D. Evaluation of Mg[B(HFIP)(4)](2)-Based Electrolyte Solutions for Rechargeable Mg Batteries. ACS Appl. Mater. Interfaces 2021, 13, 54884–54895.
- (22) Li, Y. Q.; Guan, S. L.; Huo, H.; Ma, Y. L.; Gao, Y. Z.; Zuo, P. J.; Yin, G. P. A Review of Magnesium Aluminum Chloride Complex Electrolytes for Mg Batteries. *Adv. Funct. Mater.* **2021**, *31*, No. 2100650.
- (23) Zhao-Karger, Z.; Bardaji, M. E. G.; Fuhr, O.; Fichtner, M. A New Class of Non-Corrosive, Highly Efficient Electrolytes for Rechargeable Magnesium Batteries. *J. Mater. Chem. A* **2017**, *5*, 10815–10820.
- (24) Mandai, T. Critical Issues of Fluorinated Alkoxyborate-Based Electrolytes in Magnesium Battery Applications. ACS Appl. Mater. Interfaces 2020, 12, 39135–39144.
- (25) Barile, C. J.; Spatney, R.; Zavadil, K. R.; Gewirth, A. A. Investigating the Reversibility of in Situ Generated Magnesium Organohaloalurninates for Magnesium Deposition and Dissolution. *J. Phys. Chem. C* **2014**, *118*, 10694–10699.
- (26) Shterenberg, I.; Salama, M.; Gofer, Y.; Levi, E.; Aurbach, D. The Challenge of Developing Rechargeable Magnesium Batteries. *MRS Bull.* **2014**, *39*, 453–460.
- (27) See, K. A.; Chapman, K. W.; Zhu, L. Y.; Wiaderek, K. M.; Borkiewicz, O. J.; Barile, C. J.; Chupas, P. J.; Gewirth, A. A. The Interplay of Al and Mg Speciation in Advanced Mg Battery Electrolyte Solutions. *J. Am. Chem. Soc.* **2016**, *138*, 328–337.
- (28) See, K. A.; Liu, Y. M.; Ha, Y.; Batik, C. J.; Gewirth, A. A. Effect of Concentration on the Electrochemistry and Speciation of the Magnesium Aluminum Chloride Complex Electrolyte Solution. *ACS Appl. Mater. Interfaces* **2017**, *9*, 35729–35739.
- (29) Barile, C. J.; Barile, E. C.; Zavadil, K. R.; Nuzzo, R. G.; Gewirth, A. A. Electrolytic Conditioning of a Magnesium Aluminum Chloride Complex for Reversible Magnesium Deposition. *J. Phys. Chem. C* **2014**, *118*, 27623–27630.
- (30) Aurbach, D.; Schechter, A.; Moshkovich, M.; Cohen, Y. On the Mechanisms of Reversible Magnesium Deposition Processes. *J. Electrochem. Soc.* **2001**, *148*, A1004—A1014.
- (31) Ta, K.; See, K. A.; Gewirth, A. A. Elucidating Zn and Mg Electrodeposition Mechanisms in Nonaqueous Electrolytes for Next-Generation Metal Batteries. *J. Phys. Chem. C* **2018**, *122*, 13790–13796.
- (32) Gao, T.; Hou, S.; Huynh, K.; Wang, F.; Eidson, N.; Fan, X. L.; Han, F. D.; Luo, C.; Mao, M. L.; Li, X. G.; Wang, C. S. Existence of Solid Electrolyte Interphase in Mg Batteries: Mg/S Chemistry as an Example. ACS Appl. Mater. Interfaces 2018, 10, 14767–14776.
- (33) Li, B.; Masse, R.; Liu, C. F.; Hu, Y.; Li, W. S.; Zhang, G. Q.; Cao, G. Z. Kinetic Surface Control for Improved Magnesium-Electrolyte Interfaces for Magnesium Ion Batteries. *Energy Storage Mater.* **2019**, 22, 96–104.
- (34) Aurbach, D.; Moshkovich, M.; Schechter, A.; Turgeman, R. Magnesium Deposition and Dissolution Processes in Ethereal Grignard Salt Solutions using Simultaneous EQCM-EIS and in Situ FTIR Spectroscopy. *Electrochem. Solid-State Lett.* **1999**, *3*, 31–34.

- (35) Weber, I.; Ingenmey, J.; Schnaidt, J.; Kirchner, B.; Behm, R. J. Influence of Complexing Additives on the Reversible Deposition/ Dissolution of Magnesium in an Ionic Liquid. Chemelectrochem 2021, 8, 390-402.
- (36) Tuerxun, F.; Yamamoto, K.; Hattori, M.; Mandai, T.; Nakanishi, K.; Choudhary, A.; Tateyama, Y.; Sodeyama, K.; Nakao, A.; Uchiyama, T.; Matsui, M.; Tsuruta, K.; Tamenori, Y.; Kanamura, K.; Uchimoto, Y. Determining Factor on the Polarization Behavior of Magnesium Deposition for Magnesium Battery Anode. ACS Appl. Mater. Interfaces 2020, 12, 25775-25785.
- (37) Tuerxun, F.; Yamamoto, K.; Mandai, T.; Tateyama, Y.; Nakanishi, K.; Uchiyama, T.; Watanabe, T.; Tamenori, Y.; Kanamura, K.; Uchimoto, Y. Effect of Interaction among Magnesium Ions, Anion, and Solvent on Kinetics of the Magnesium Deposition Process. J. Phys. Chem. C 2020, 124, 28510-28519.
- (38) Wang, H.; Feng, X. F.; Chen, Y.; Liu, Y. S.; Han, K. S.; Zhou, M. X.; Engelhard, M. H.; Murugesan, V.; Assary, R. S.; Liu, T. L.; Henderson, W.; Nie, Z. M.; Gu, M.; Xiao, J.; Wang, C. M.; Persson, K.; Mei, D. H.; Zhang, J. G.; Mueller, K. T.; Guo, J. H.; Zavadil, K.; Shao, Y. Y.; Liu, J. Reversible Electrochemical Interface of Mg Metal and Conventional Electrolyte Enabled by Intermediate Adsorption. ACS Energy Lett. 2020, 5, 200-206.
- (39) Sigalov, S.; Shpigel, N.; Levi, M. D.; Feldberg, M.; Daikhin, L.; Aurbach, D. Electrochemical Quartz Crystal Microbalance with Dissipation Real-Time Hydrodynamic Spectroscopy of Porous Solids in Contact with Liquids. Anal. Chem. 2016, 88, 10151-10157.
- (40) Shpigel, N.; Levi, M. D.; Aurbach, D. EQCM-D Technique for Complex Mechanical Characterization of Energy Storage Electrodes: Background and Practical Guide. Energy Storage Mater. 2019, 21, 399-413.
- (41) Kitz, P. G.; Lacey, M. J.; Novak, P.; Berg, E. J. Operando EQCM-D with Simultaneous in Situ EIS: New Insights into Interphase Formation in Li Ion Batteries. Anal. Chem. 2019, 91, 2296-2303.
- (42) Cora, S.; Ahmad, S.; Sa, N. Y. In Situ Probing of Mass Exchange at the Solid Electrolyte Interphase in Aqueous and Nonaqueous Zn Electrolytes with EQCM-D. ACS Appl. Mater. Interfaces 2021, 13, 10131-10140.
- (43) Mizrahi, O.; Amir, N.; Pollak, E.; Chusid, O.; Marks, V.; Gottlieb, H.; Larush, L.; Zinigrad, E.; Aurbach, D. Electrolyte Solutions with a Wide Electrochemical Window for Recharge Magnesium Batteries. J. Electrochem. Soc. 2008, 155, A103-A109.
- (44) Yagi, S.; Tanaka, A.; Ichikawa, Y.; Ichitsubo, T.; Matsubara, E. Electrochemical Stability of Magnesium Battery Current Collectors in a Grignard Reagent-Based Electrolyte. J. Electrochem. Soc. 2013, 160, C83-C88.
- (45) Lipson, A. L.; Han, S. D.; Pan, B.; See, K. A.; Gewirth, A. A.; Liao, C.; Vaughey, J. T.; Ingram, B. J. Practical Stability Limits of Magnesium Electrolytes. J. Electrochem. Soc. 2016, 163, A2253-A2257.
- (46) Pour, N.; Gofer, Y.; Major, D. T.; Aurbach, D. Structural Analysis of Electrolyte Solutions for Rechargeable Mg Batteries by Stereoscopic Means and DFT Calculations. J. Am. Chem. Soc. 2011, 133, 6270-6278.
- (47) Bard, A. J.; Faulkner, L. R. Electrochemical Methods: Fundamentals and Applications, 2nd ed.; John Wiley & Sons, Inc.: New York, 2001.
- (48) Castro, P.; Resa, P.; Elvira, L. Apparent Negative Mass in QCM Sensors Due to Punctual Rigid Loading. IOP Conf. Ser.: Mater. Sci. Eng. 2012, 42, No. 012046.
- (49) Shpigel, N.; Levi, M. D.; Sigalov, S.; Girshevitz, O.; Aurbach, D.; Daikhin, L.; Jackel, N.; Presser, V. Non-Invasive In Situ Dynamic Monitoring of Elastic Properties of Composite Battery Electrodes by EQCM-D. Angew. Chem., Int. Ed. 2015, 54, 12353-12356.
- (50) Dargel, V.; Shpigel, N.; Sigalov, S.; Nayak, P.; Levis, M. D.; Daikhin, L.; Aurbach, D. In Situ Real-Time Gravimetric and Viscoelastic Probing of Surface Films Formation on Lithium Batteries Electrodes. Nat. Commun. 2017, 8, No. 1389.

- (51) Seki, T.; Chiang, K. Y.; Yu, C. C.; Yu, X. Q.; Okuno, M.; Hunger, J.; Nagata, Y.; Bonn, M. The Bending Mode of Water: A Powerful Probe for Hydrogen Bond Structure of Aqueous Systems. J. Phys. Chem. Lett. 2020, 11, 8459-8469.
- (52) Dwivedi, A.; Baboo, V.; Bajpai, A. Fukui Function Analysis and Optical, Electronic, and Vibrational Properties of Tetrahydrofuran and Its Derivatives: A Complete Quantum Chemical Study. J. Theor. Chem. 2015, 2015, No. 345234.
- (53) Dubouis, N.; Lemaire, P.; Mirvaux, B.; Salager, E.; Deschamps, M.; Grimaud, A. The Role of the Hydrogen Evolution Reaction in the Solid-Electrolyte Interphase Formation Mechanism for "Water-in-Salt" Electrolytes. Energy Environ. Sci. 2018, 11, 3491-3499.
- (54) Kam, W.; Liew, C.-W.; Lim, J. Y.; Ramesh, S. Electrical, Structural, and Thermal Studies of Antimony Trioxide-Doped Poly(Acrylic Acid)-Based Composite Polymer Electrolytes. Ionics 2014, 20, 665-674.
- (55) Ha, S.-Y.; Lee, Y.-W.; Woo, S. W.; Koo, B.; Kim, J.-S.; Cho, J.; Lee, K. T.; Choi, N.-S. Magnesium(II) Bis(Trifluoromethane Sulfonyl) Imide-Based Electrolytes with Wide Electrochemical Windows for Rechargeable Magnesium Batteries. ACS Appl. Mater. Interfaces 2014, 6, 4063-4073.

□ Recommended by ACS

Integration of PDAAQ and Non-stoichiometric MgO as Host Cathode Materials for Lithium-Sulfur Batteries with Superior Cycle Stability: Density Functional Theory Calcu...

Maryam Sadat Kiai, Rakesh K Sharma, et al.

NOVEMBER 30, 2022 **ENERGY & FUELS**

RFAD 🗹

MgAl Saponite as a Transition-Metal-Free Anode Material for Lithium-Ion Batteries

Jian Zhang, Jingbin Han, et al.

DECEMBER 02, 2022

ACS APPLIED MATERIALS & INTERFACES

READ **C**

Reversibility of a High-Voltage, Cl-Regulated, Aqueous Mg Metal Battery Enabled by a Water-in-Salt Electrolyte

Kee Wah Leong, Dennis Y. C. Leung, et al.

JULY 21, 2022

ACS ENERGY LETTERS

RFAD 17

Charge-Discharge Properties of Sputtered Mg Anode in Flexible All-Solid-State Mg-Ion Batteries

Kuan-Jen Chen, Yen-Ting He, et al.

NOVEMBER 14, 2022

ACS OMEGA

READ **C**

Get More Suggestions >